Hydrodynamically Driven Colloidal Assembly in Dip Coating

Carlos E. Colosqui, Jeffrey F. Morris, and Howard A. Stone

Hydrodynamically-driven colloidal assembly in dip coating

Carlos E. Colosqui and Jeffrey F. Morris

Benjamin Levich Institute, City College of the City

University of New York, New York, NY 10031, USA

Howard A. Stone[*]

Department of Mechanical and Aerospace Engineering,

Princeton University, Princeton, NJ 08544, USA

Abstract

We study the hydrodynamics of dip coating from a suspension and report a mechanism for colloidal assembly and pattern formation on smooth substrates. Below a critical withdrawal speed where the coating film is thinner than the particle diameter, capillary forces induced by deformation of the free surface prevent the convective transport of single particles through the meniscus beneath the film. Capillary-induced forces are balanced by hydrodynamic drag only after a minimum number of particles assemble within the meniscus. The particle assembly can thus enter the thin film where it moves at nearly the withdrawal speed and rapidly separates from the next assembly. The interplay between hydrodynamic and capillary forces produces periodic and regular structures below a critical ratio $Ca^{2/3}/\sqrt{Bo} < 0.7$ where Ca and Bo are the capillary and Bond numbers, respectively. An analytical model and numerical simulations are presented for the case of two-dimensional flow with circular particles in suspension. The hydrodynamically-driven assembly documented here is consistent with stripe pattern formations observed experimentally in dip coating.

The ability to build crystalline microstructures on smooth substrates enables significant advances in materials science and microfabrication, e.g. optoelectronics and metamaterials [1, 2]. Film formation from a colloidal suspension, via substrate withdrawal and/or solvent evaporation, can produce patterned microstructures that extend over millimeter lengths [3–6]. For example, experimental studies have demonstrated a critical withdrawal speed below which the periodicity and regularity of the structures increase dramatically [5, 6]. The critical speed corresponded to the conditions at which the particle diameter is equal to the thickness of a thin coating film predicted by the Landau-Levich theory [7] and set the upper limit of the so-called thin-film entrainment regime [5]. In this regime, the formation of periodic stripe patterns has been observed on partially wetting substrates [5] and further studied on hydrophilic substrates [6]. These experimental studies report that (i) very low particle concentrations are required for the formation of regular assemblies, and (ii) varying the withdrawal speed has a much greater effect on the stripe morphology than varying the solvent evaporation rate. The employed technique, referred to as convective self-assembly (CSA), involves convective transport of colloidal particles from the bulk of the solution to the meniscus and coating film.

Under conditions where the assembly process takes place, the energies of convective motions and capillary interactions are much larger than the thermal energy $k_B T$ (here k_B is the Boltzmann constant, and T is the absolute temperature) and Brownian effects may be neglected. Self-organization processes in CSA can thus be strongly influenced by hydrodynamic interactions between colloidal particles. Previous studies, however, attributed the stripe pattern formation to mechanisms that only consider capillary interactions and quasi-static processes [5, 6]. In this Letter, we study and document the critical role of hydrodynamic effects in the particle assembly and subsequent pattern formation.

To study the hydrodynamics of the fluid-particle system, we employ a class of lattice Boltzmann (LB) methods for isothermal multiphase flow [8–11] that is combined with an immersed boundary (IB) approach [12]. The employed IB approach represents the solid phase with a smooth distribution function $\Phi_S(\mathbf{x}, t) \in [0, 1]$ [see Fig. 1(a) and Supplemental Material]. We adjust fluid-solid interactions in our model so that solid phases are completely wetted by the liquid phase. Also, we neglect long-range molecular interactions between solid bodies and thermal fluctuations that produce Brownian effects.

The numerical model is applied to study the dynamics of colloidal assembly during dip

2

coating from a suspension of neutrally buoyant particles. Dip coating of plates produces a nearly two-dimensional flow that drives the convective transport of particles from the suspension bulk to the meniscus region and subsequently to the coating film. Furthermore, the formation of regular stripes [3, 5, 6] requires a statistically homogeneous distribution of particles along the direction of the stripes. We proceed by studying a two-dimensional flow configuration that resembles the Landau-Levich problem [7] of plate coating via withdrawal from a liquid bath, where we later introduce circular particles. With these simplifications we capture the basic mechanisms of particle assembly and stripe formation.

Dimensional analysis of the problem yields three dimensionless groups; these are the capillary number, Ca, the Bond number, Bo, and the Reynolds number, Re. We define $Ca = U\mu/\gamma$ where U is the withdrawal speed, μ is the viscosity of the liquid, and γ is the liquid-vapor surface tension. The Bond number is $Bo = (R/\ell_c)^2$ where R is the particle radius and $\ell_c = \sqrt{\gamma/g\Delta\rho}$ is the capillary length determined by the gravitational acceleration, g, and the density contrast between the liquid and vapor phases, $\Delta\rho$. The physical conditions in our numerical simulations correspond to low capillary numbers $Ca \simeq 0.01$–0.08 and a small Bond number $Bo = 6 \times 10^{-3}$. The resulting particle dynamics are characterized by small Reynolds numbers $Re = \rho U R/\mu \simeq 0.075$–$0.3$ (here ρ is the liquid density), which justifies neglecting inertial effects. For these conditions the coating film thickness, h_f, is smaller than the particle diameter, $2R$, which correspond to the regime where pattern formation can be observed in experiments [3–6].

We perform numerical simulations in a rectangular domain that is partially bounded by a moving wall (i.e., the withdrawn substrate) and three stationary walls. At initialization, the liquid bath lies below the level y_H indicated Fig. 1(a). The simulated pressure/temperature conditions produce a negligible evaporation rate of the liquid solvent. Particles in varying numbers, from zero to twenty, are released at the same time with zero initial velocity from different locations within the left half of the liquid bath (nearest the moving wall). Details of the simulation procedures are provided in the Supplemental Material.

First, we study the background flow topology via simulations without particles. The steady-state flow topology, reported in Fig. 1(a), is typically observed in dip coating [13]. A fundamental feature of this flow configuration is the presence of a stagnation point S* on the vapor-liquid interface at vertical position $y = y^*$ [Fig. 1(a)]. The flow streamline ending at S* defines the boundary between a "shear flow" region, $\Gamma 1$, which continues into
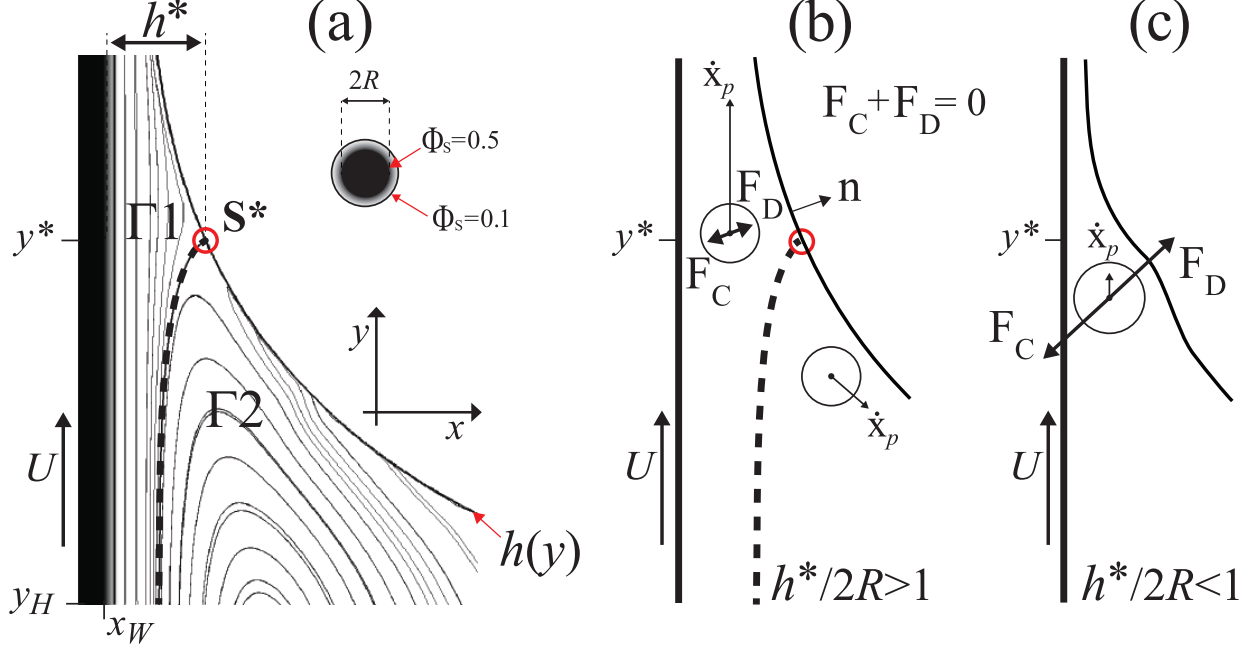
FIG. 1. Flow topology and forces on a completely wetted particle. (a) Streamlines within the meniscus (Ca=0.04). A stagnation point S* (circle) lies on the interface where $h(y^*)=h^*$. The streamline (dashed line) ending at S* separates a "shear flow" region, $\Gamma 1$, from a "recirculation flow" region, $\Gamma 2$. The surface of the withdrawn substrate is at $x=x_W$ and the horizontal level of the bath (at initialization) is at $y=y_H$. A simulated particle is illustrated for reference; the diffuse fluid-solid interface is centered at $\Phi_S(\mathbf{x},t)$=0.5. (b) Forces on a particle for $h^*/2R > 1$; $\mathbf{F}_C$ is the capillary-induced force and $\mathbf{F}_D$ is the effective drag. (c) Forces on a particle for $h^*/2R < 1$.

the coating film, and a "recirculation flow" region, $\Gamma 2$, which extends into the liquid bath. Above the meniscus, the film thickness in numerical simulations agrees within 5–10% with analytical predictions, $h_f/\ell_c = 0.95\ Ca^{2/3} - 0.1\ Ca$, valid for $Ca \leq 0.1$ [7]. More importantly, the meniscus thickness $h(y^*) = h^*$ observed at the stagnation point agrees well with the expression $h^*/\ell_c = [3(h_f/\ell_c) - (h_f/\ell_c)^3/Ca]$ based on lubrication theory [7].

Given the flow topology in Fig. 1(a) we observe that $h^* > 2R$ appears to be critical for a particle to enter the film. Normalizing h^* by the particle diameter this entrainment condition is equivalent $h^*/2R \simeq 1.42Ca^{2/3}/\sqrt{Bo} > 1$. As illustrated in Figs. 1(b–c), we consider a completely wetted and neutrally buoyant particle moving at velocity $\dot{\mathbf{x}}_p = \dot{x}_p\mathbf{i} + \dot{y}_p\mathbf{j}$ and assume a negligible angular velocity $\dot{w}_p \ll |\dot{\mathbf{x}}_p|/R$. The particle experiences an effective drag, $\mathbf{F}_D$, and a capillary-induced force, $\mathbf{F}_C$, due to local deformation of the interface.

4

Neglecting small inertial effects for $Re \ll 1$ we have $\mathbf{F}_C + \mathbf{F}_D = \mathbf{0}$. Since $\mathbf{F}_C$ acts normal to the interface and increases with the interfacial deformation, so must the effective drag force responsible for driving the particle towards the film. For $h(y)/2R \lesssim 1$ the vertical component of the drag is $\mathbf{F}_D \cdot \mathbf{j} \propto (U - \dot{y}_p)$ and the effective drag increases as the particle speed decreases. When $h^*/2R > 1$ [cf. Fig. 1(b)], capillary forces in the vertical direction are small and thus $\dot{y}_p \simeq U$; particles within $\Gamma 2$ return to the bath. When $h^*/2R < 1$ and inside the meniscus $y \leq y^*$ [cf. Fig. 1(c)], large interfacial deformations yield large capillary forces in the vertical direction and thus $\dot{y}_p < U$; the particle is prevented from entering the film in the limit $\dot{y}_p \rightarrow 0$.

To verify the above analysis, we study numerically the center-of-mass trajectories $\{x_p(t), y_p(t)\}$ of particles released after the background flow in Fig. 1(a) is established. Single particles released within the "recirculation flow" region $\Gamma 2$ attain stable orbits within the bath that prevent them from entering the film (see Supplemental Material). The case of a single particle (p=I) released within the "shear flow" region $\Gamma 1$ is of particular interest. Indeed, when the withdrawal speed is sufficiently large so that $h^*/2R > 1$ single particles successfully enter the film. When approaching the film, the trajectories within $\Gamma 1$ are compressed into a unique "entrainment" trajectory. The vertical speed is dominant along the entrainment trajectory; i.e. $|\dot{x}_I|/|\dot{y}_I| \lesssim 0.1$ and $|\dot{w}_I R|/|\dot{y}_I| \lesssim 0.75$. The vertical displacements $\Delta y = y_I(t) - y_H \geq 0$ for different withdrawal speeds corresponding to $h^*/2R = 1.3$–3 ($Ca = 0.02$–0.08) are reported in Fig. 2(a). A significant variation in the particle speed $\dot{y}_I = dy_I/dt$ can be observed in Fig. 2(a): the speed is nearly constant ($\dot{y}_I \simeq 0.65U$) below the meniscus ($y_I \lesssim y^*$), decreases inside the meniscus ($y_I \simeq y^*$), and then increases after clearing the meniscus and entering the flat film ($y_I \gtrsim y^*$). The minimum vertical speed is reached near the stagnation point initially located at y^*.

As seen in Figs. 2(b–e), the entrainment of a single particle occurs along a nearly one-dimensional trajectory and is accompanied by significant deformation of the meniscus and flow streamlines. Considering these numerical observations we further analyze the force balance $\mathbf{F}_C + \mathbf{F}_D = \mathbf{0}$ where $\dot{y}_I \geq 0$. In the horizontal direction, while $\dot{x}_I \simeq 0$, capillary-induced forces are mainly balanced by a high pressure within the particle-wall gap. In the vertical direction, drag forces driving the translational motion are counteracted by capillary-induced forces. For a confined particle moving parallel to a wall, the vertical component of the drag may be expressed as $F_D = -\mu(K_I \dot{y}_I - K_U U)$ where $K_I > 0$ and $K_U > 0$ are local
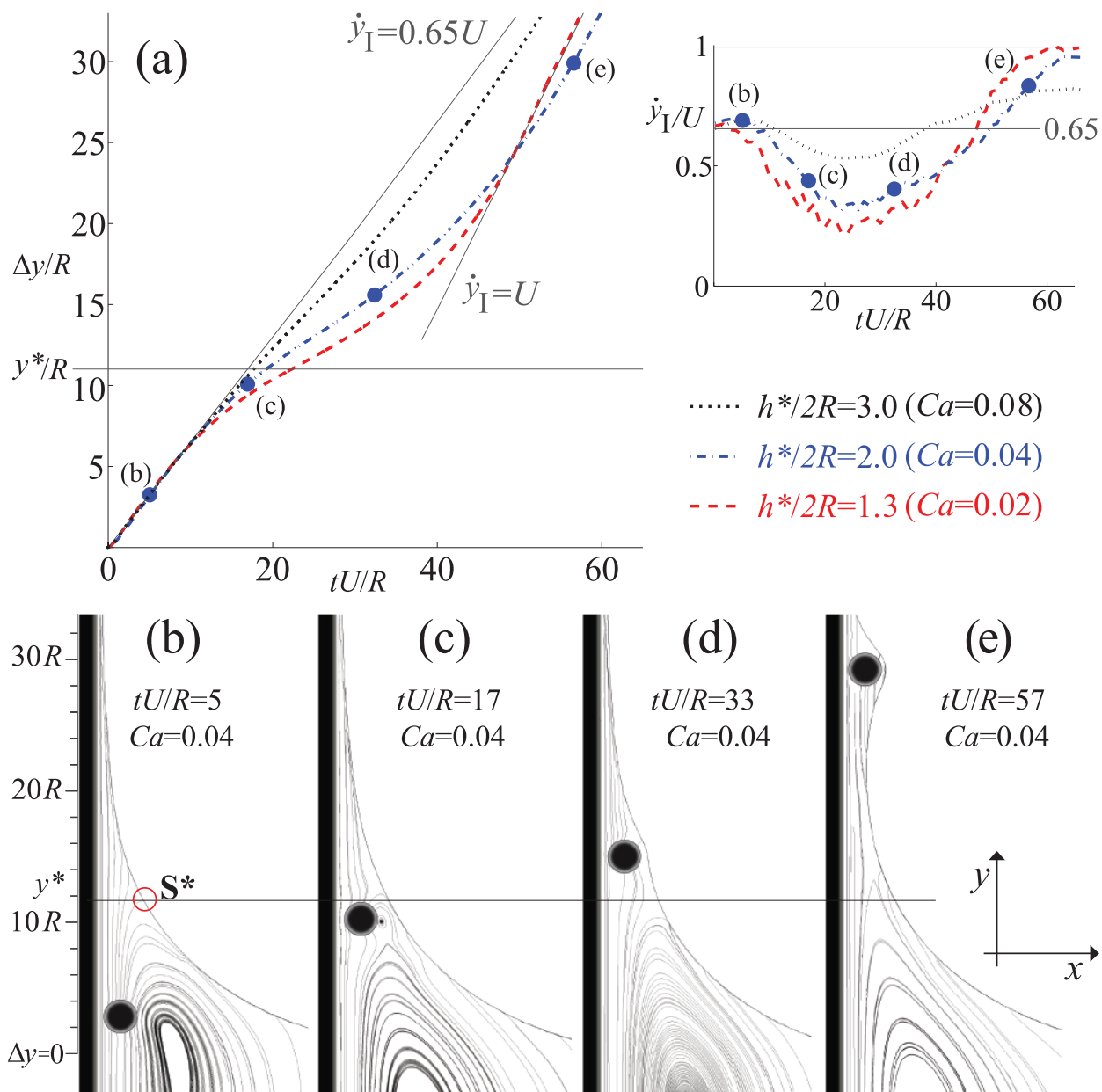
FIG. 2. Single particle dynamics for $h^*/2R > 1$. (a) Vertical displacement $\Delta y = y_I(t) - y_H$ vs. tU/R, the straight lines and inset show the vertical speed $\dot{y}_I = dy_I/dt$. The time origin ($t = 0$) is chosen so that $\Delta y(0) = 0$. For $\Delta y > 0$ individual particles released within $\Gamma 1$ follow a common xy-trajectory at a given Ca. (b–e) Streamlines for $h^*/2R = 2$ ($Ca = 0.04$) at different time instances indicated in panel (a).

resistance coefficients. The ratio of resistances $f_D = K_U/K_I \to 0$ for low confinement and far from the wall ($h/2R \gg 1$), while $f_D \sim 1$ in high confinement and close to the wall ($h \lesssim 2R$) where the drag law becomes $F_D \simeq -\mu K_I(\dot{y}_I - U)$. For $Bo \ll 1$, we consider that capillary forces act normal to the interface with their magnitude determined by a shape function $f_C(h/2R) = |F_C|/\gamma$. The vertical component of the capillary-induced force (per unit length) is $F_C = \gamma f_C(h/2R)(h_y/\sqrt{1 + |h_y|^2})$ where $h_y \equiv dh/dy$. Neglecting inertial effects of order $\mathcal{O}(Re)$ we obtain

$$\frac{\dot{y}_I}{U} = f_D(h/2R) + \frac{f_C(h/2R)}{K_I Ca} \frac{dh/dy}{\sqrt{1 + |dh/dy|^2}} \tag{1}$$

where $f_D > 0$ and $f_C > 0$ are positive functions of the ratio $h(y)/2R$. Hence, Eq. (1) predicts a decay in vertical speed within the meniscus where $dh/dy < 0$; this capillary effect increases for small Ca. Once inside the film, we have $dh/dy \simeq 0$ while $f_D \to 1$ in high confinement, and thus the particle speed increases, $\dot{y}_I \to U$.

Moreover, Eq. (1) predicts that particles can be stopped within the meniscus below a critical value of the ratio $h(y^*)/2R$. Geometric analysis of the interfacial deformation for $h^* \lesssim 2R$ yields $f_C(h^*/2R) = 2\sqrt{1 - h^*/2R}$, while an approximate solution of the thickness profile [7] gives $dh(y^*)/dy \simeq -3Ca^{1/3}$ (see Supplemental Material). For $\dot{y}_I = 0$ and $y_I = y^*$, Eq.(1) yields $h^*/2R \simeq 1 - (K_I/6)^2 Ca^{4/3}$. This critical condition to stop a particle within the meniscus is equivalent to $h^*/2R \simeq 1$ for $Ca \ll 1$. Indeed, simulation results in Fig. 3 for a low withdrawal speed, where $h^*/2R = 0.8$ ($Ca = 0.01$), show that a single particle can attain a stationary position within the meniscus.

Eq. (1) indicates, through the functions f_D and f_C, that widening and/or flattening the meniscus has significant effects on the particle speed. For $y \simeq y^*$ we observe that $\dot{y}_I \to 0$ as $h^*/2R \to 0$. If a particle at $y \simeq y^*$ widens the meniscus [cf. Fig. 2(e)], a particle below y^* may be dragged by the flow at a faster vertical speed.

Simulations with multiple particles confirm a flow-driven assembly below the film for $h^*/2R = 0.8$. Three particles (p=I-II-III) in one case [cf. Fig. 4(a)] and two particles (p=I-III) in a second case [cf. Fig. 4(b)] are released simultaneously with initial separations $y_I - y_{II} = 3R$ and $y_I - y_{III} = 9R$ where $y_I(0) \simeq y_H$. The vertical displacements in Fig. 4(a) show that the trailing particle (III) climbs faster than the leading particles (I-II). In both cases the particles reduce their initial separations and assemble inside the meniscus [cf. Figs. 4(c–e) and Figs. 4(f–g)]. Below the critical condition $h^*/2R < 1$, a minimum
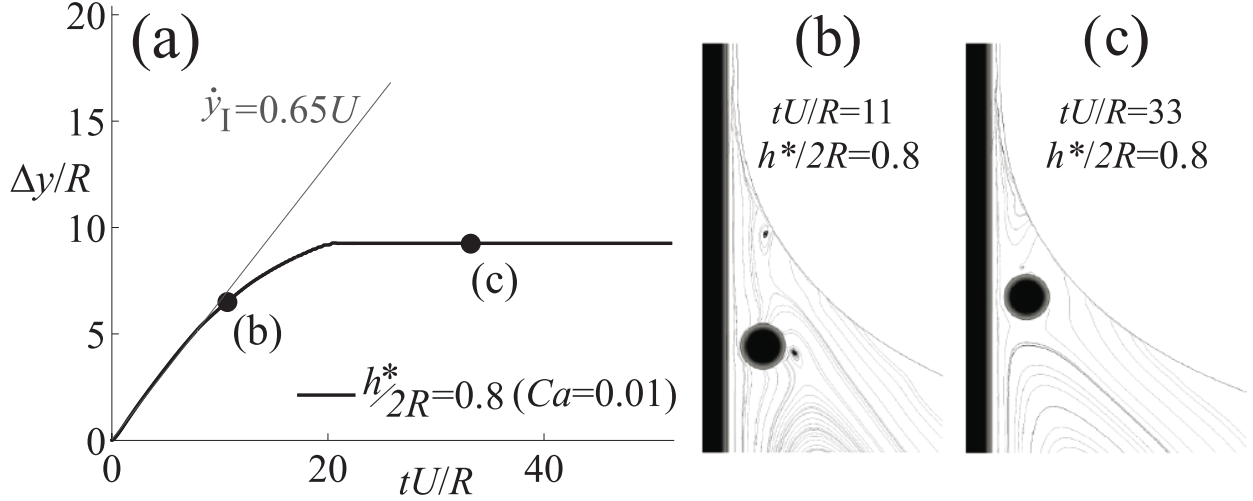
FIG. 3. Single particle dynamics for $h^*/2R < 1$. (a) Vertical displacement $\Delta y = y_I(t) - y_H$ vs. tU/R for $h^*/2R = 0.8$ ($Ca = 0.01$). The time origin ($t = 0$) is chosen so that $\Delta y(0) = 0$. Single particles released within $\Gamma 1$ reach a steady position inside the meniscus; $\dot{y}_I = 0$ for $tU/R > 25$. (b–c) Streamlines at the two times indicated in panel (a).

number of colloidal particles (three in the studied conditions) must assemble in a close-packed formation before film entrainment is possible. A close packing of particles increases the vertical drag and flattens the local interface curvature so that $dh/dy \to 0$ for particles inside the assembly. When the effective hydrodynamic drag balances the forces induced by interfacial deformation, the particle assembly enters the film and increases its speed as seen in Figs. 4(c–e).

Simulations with larger numbers of particles ($N_p = 10$–20) further corroborate the periodic formation of regular assemblies when $h^*/2R < 1$ [cf. Fig. 5(a)]. To draw this conclusion, we performed five realizations of each numerical simulation by releasing particles from random locations with root-mean-square particle separations $|\Delta \mathbf{x}_{rms}| = 3.5R$ and $|\Delta \mathbf{x}_{rms}| = 2.5R$, which corresponds to area fractions $\phi = 0.13$ and $\phi = 0.25$ respectively. For $h^*/2R < 1$ and the lower area fraction $\phi = 0.13$ [cf. Fig. 5(a)], particle assemblies fully form before entering the film, which in turn enhances the periodicity and regularity of the arrays (see movies included with the Supplemental Material). As seen in Figs. 5(b–c), increasing the area fraction or the withdrawal speed produces irregular assemblies that form once within the coating film. In this case, a different mechanism due to long-ranged capillary interactions and film instabilities [1] drives the assembly, which deteriorates the periodicity and regularity
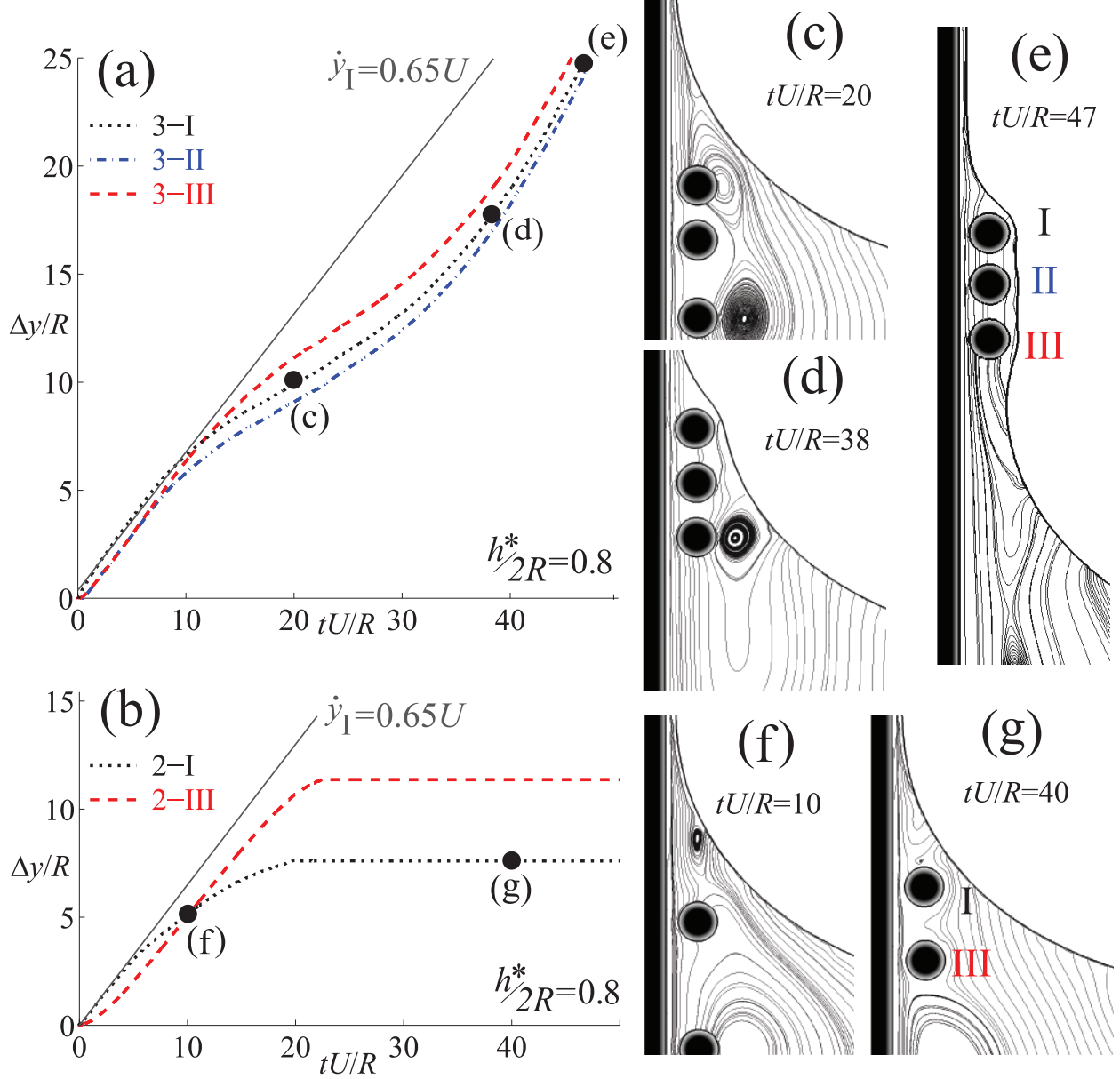
8

FIG. 4. Hydrodynamically-driven assembly for $h^*/2R = 0.8$ ($Ca = 0.01$). (a–b) Vertical displacement $\Delta y_p = y_p(t) - y_p(0)$ vs. tU/R. Three (p=I-II-II) and two (p=I-II) particles are released at $t = 0$; $y_{II}(0) = y_I(0) - 3R$, $y_{III}(0) = y_I(0) - 6R$, and $y_I(0) \simeq y_H$. (c–e) and (f–g) Streamlines at time instances indicated in panels (a) and (b).

of the observed arrays.

In conclusion, our study indicates that below a critical condition $h^* < 2R$, or equivalently $Ca^{2/3}/\sqrt{Bo} < 0.7$, colloidal particles can assemble inside the meniscus producing highly regular structures. Our results are relevant to physical conditions where $Re \ll 1$,
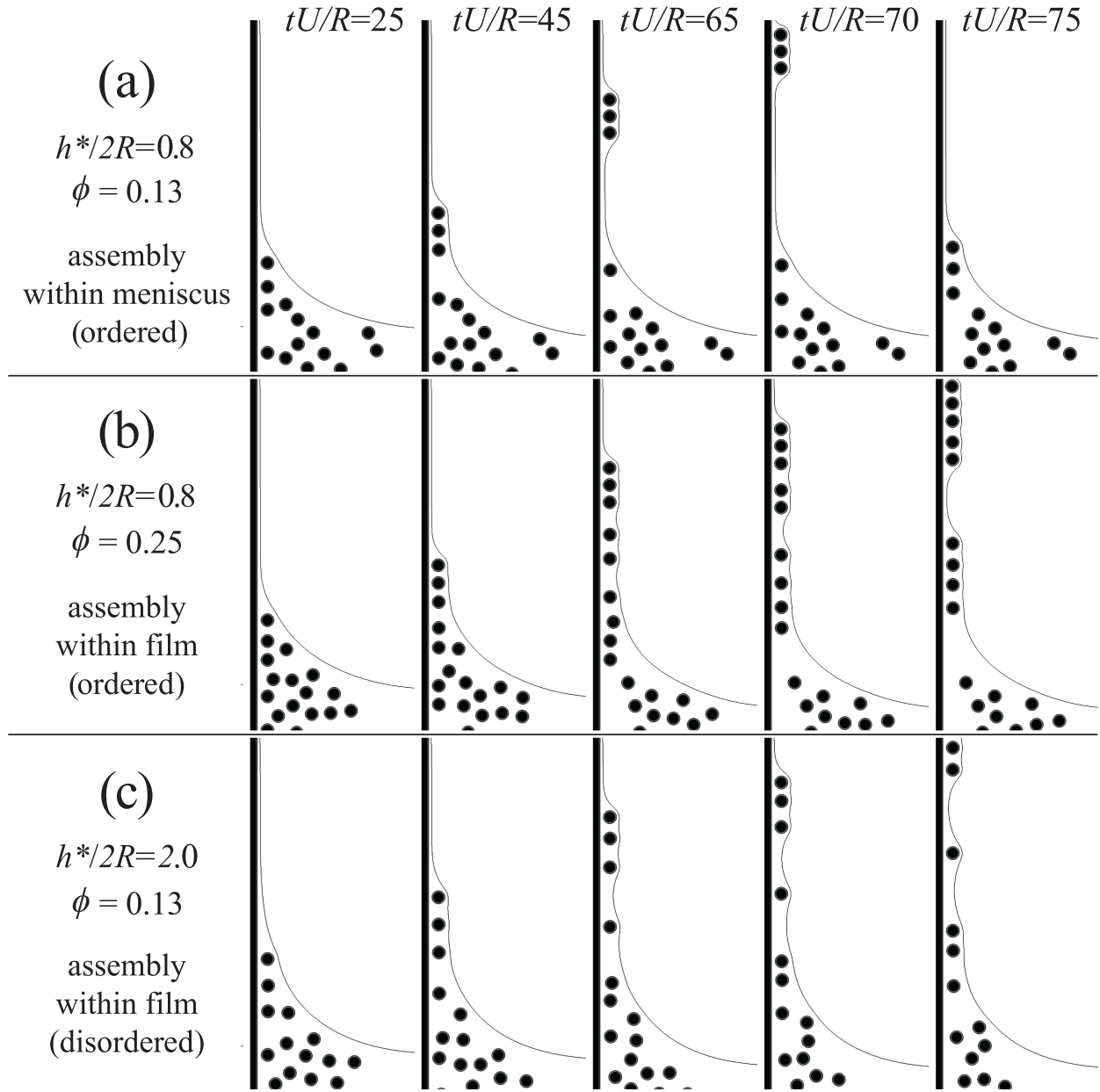
9

FIG. 5. Stripe formation and transition to disorder. Each sequence shows six time instances for (a) $h^*/2R$=0.8 and ϕ=0.13, (b) $h^*/2R$=0.8 and ϕ=0.25, and (c) $h^*/2R$=2.0 and ϕ=0.13. For $h^*/2R < 1$ ($Ca \lesssim 0.6Bo^{3/4}$) and low area fraction (ϕ=0.13) the assembly occurs inside the meniscus, which increases order and periodicity (see movies in Supplemental Material). For $h^*/2R > 1$ we observe disordered arrays.

$Ca \ll 1$, and $Bo \ll 1$. We consider a balance between viscous drag and forces induced by deformation of the interface; hydrodynamic interactions between particles thus have critical effects. The identified assembly mechanism differs from others previously proposed that can dominate under different conditions [5, 6]. Our simulations and analysis agree with experimental observations of a transition from disordered deposition to stripe pattern formation on thin coating films $h_f < 2R$ [5, 6]. Further quantitative studies of array morphology require matching dimensionless groups and volume fractions employed in experimental conditions, which entails intensive computational resources. The results in this Letter provide better fundamental understanding that could improve current technologies for the flow-driven assembly of colloidal crystals.

———————

* hastone@princeton.edu

[1] P. Kralchevsky and K. Nagayama, *Particles at Fluids Interfaces and Membranes*, Vol. 10 (Elsevier Science, 2001).

[2] K. Stebe, E. Lewandowski, and M. Ghosh, Science **325**, 159 (2009).

[3] O. Giraldo, J. Durand, H. Ramanan, K. Laubernds, S. Suib, M. Tsapatsis, S. Brock, and M. Marquez, Angew. Chem. **115**, 3011 (2003).

[4] M. Abkarian, J. Nunes, and H. A. Stone, J. Am. Chem. Soc. **126**, 5978 (2004).

[5] M. Ghosh, F. Fan, and K. Stebe, Langmuir **23**, 2180 (2007).

[6] S. Watanabe, K. Inukai, S. Mizuta, and M. Miyahara, Langmuir **25**, 7287 (2009).

[7] L. Landau and B. Levich, Acta Physicochim. URSS **17** (1942); S. Wilson, J. Eng. Math. **16**, 209 (1982).

[8] X. Shan and H. Chen, Phys. Rev. E **47**, 1815 (1993).

[9] C. E. Colosqui, Phys. Rev. E **81**, 026702 (2010).

[10] R. Benzi, S. Chibbaro, and S. Succi, Phys. Rev. Lett. **102**, 026002 (2009); R. Benzi, S. Succi, and M. Vergassola, Phys. Rep. **222**, 145 (1992).

[11] C. E. Colosqui, M. E. Kavousanakis, A. G. Papathanasiou, and I. G. Kevrekidis, Phys. Rev.

E **87**, 013302 (2013); C. E. Colosqui, G. Falcucci, S. Ubertini, and S. Succi, Soft Matter **8**, 3798 (2012).

[12] C. Peskin, Acta Numer. **11**, 479 (2002); R. Mittal and G. Iaccarino, Annu. Rev. Fluid Mech. **37**, 239 (2005).

[13] B. Scheid, J. Delacotte, B. Dollet, E. Rio, F. Restagno, E. A. van Nierop, I. Cantat, D. Langevin, and H. A. Stone, Europhys. Lett. **90**, 24002 (2010).